JOURNAL OF PROPULSION AND POWER
Vol. 13, No. 5, September–October 1997

Applications of Algebraic Reynolds Stress Turbulence Models Part 1: Incompressible Flat Plate

John R. Carlson*
NASA Langley Research Center, Hampton, Virginia 23681

The ability of the three-dimensional Navier–Stokes method, PAB3D, to simulate the effect of Reynolds number variation by using nonlinear explicit algebraic Reynolds stress turbulence modeling was assessed. Subsonic flat-plate boundary-layer flow parameters such as law-of-the-wall velocity distributions, local and average skin friction, skin friction correlation, and shape factors were compared with direct numerical simulation calculations and classical theory at local Reynolds numbers up to 180 × 10^6. Each model displayed slightly different low and high Reynolds number characteristics, but generally compared very well with classical theories and data. No definitive advantage of one explicit algebraic Reynolds stress model over another was observed.

Nomenclature

C_F = average skin friction coefficient, $(1/lq_\infty)\ \Sigma\ \tau_w \Delta l$
c_f = local skin friction coefficient, τ_w/q_∞
F = axial force along body axis
f_μ = near-wall damping function for linear K-ε
H_{12} = boundary-layer shape factor, δ_1/δ_2
H_{32} = boundary-layer shape factor, δ_3/δ_2
h_1 = physical height of first computational grid from a wall
K = turbulent kinetic energy
l = integration length of flat plate
M = Mach number
N_l = number of points for von Kármán constant least-squares fit
n = direction normal to wall
$\bar{P}$ = production term for turbulent kinetic energy
p = static pressure, Pa
q = dynamic pressure, Pa
R = Reynolds number based on model reference length
R_L = Reynolds number based on flat-plate integration length
R_T = cell turbulent Reynolds number, $K^2/\nu\varepsilon$
R_x = Reynolds number based on distance x, $u_\infty x/\nu$
R_{δ_1} = displacement thickness Reynolds number, $u_\infty \delta_1/\nu$
R_θ = momentum thickness Reynolds number, $u_\infty \delta_2/\nu$
S = strain tensor
t = time
$\bar{U}$ = magnitude of local velocity, $\sqrt{\Sigma\ u_k^2}$
u = streamwise velocity
u_k = Cartesian velocity components
u_τ = friction velocity, $\sqrt{(\tau_w/\rho)}$
u^+ = law-of-the-wall coordinate, u/u_τ
$u'v'$ = shear stress
$u'v'^+$ = nondimensional shear stress, $u'v'/u_\tau^2$
W = vorticity tensor
x = streamwise distance
y^+ = law-of-the-wall coordinate, nu_τ/ν
y_1^+ = law-of-the-wall height of first cell
z = vertical distance
Δl = incremental distance on flat plate
δ_1 = boundary-layer displacement thickness
δ_2 = boundary-layer momentum thickness
δ_3 = boundary-layer energy thickness
ε = turbulent dissipation
κ = von Kármán constant
μ = laminar viscosity
μ_t = turbulent viscosity
μ_w = local laminar viscosity at wall
ν = kinematic viscosity, μ/ρ
ρ = density
τ = shear stress
ϕ = angular location of pressure orifices, deg

Subscripts
l = laminar
n = nonlinear component
t = turbulent
t_0 = freestream total condition
w, wall = condition at wall surface
∞ = freestream condition

Superscripts
L = laminar
T = turbulent

Introduction

RECENTLY, the capabilities of application level three-dimensional Reynolds-averaged Navier–Stokes (RANS) methods have increased because of the rapid growth of the speed and size of computational resources concurrent with advances in turbulence modeling. Several years ago, the requirements of more completely resolving jet-shear flow physics pushed a few RANS methods to implement two-equation turbulence models. The two-equation K-ε turbulence models, though a step beyond the previous zero-, half-, and one-equation models, still make significant compromises that result in errors in the flow simulations. Theories for higher-order turbulence models have been presented for some time[1]; however, more recent efforts,[2,3] which developed the explicit algebraic Reynolds stress turbulence models, were a significant step in getting these models into the general three-dimensional Navier–Stokes methods that are presently in use. In addition,

---

Presented as Paper 96-2544 at the AIAA/ASME/SAE/ASEE 32nd Joint Propulsion Conference, Lake Buena Vista, FL, July 1–3, 1996; received Aug. 20, 1996; revision received May 7, 1997; accepted for publication May 7, 1997.

*Senior Scientist, Aero- and Gasdynamics Division, M/S 286.

these models have only had a minor additional impact to the overall computational effort and have resolved some of the errors of the linear turbulence models.

Additionally, many current projects are considering Reynolds number scaling a significant aspect of aircraft testing and development. Wing aerodynamics and flow about propulsion systems can have considerable sensitivity to varying Reynolds numbers. Most of the subscale wind-tunnel tests occur at Reynolds numbers below that of flight conditions; therefore, the ability of computational fluid dynamics (CFD) to simulate higher Reynolds number flow is of importance.

The current investigation assesses the capability of the Navier–Stokes method PAB3D version 13S (Refs. 4–7) that uses explicit algebraic Reynolds stress turbulence models to simulate a 5-m flat plate at very high Reynolds numbers. Boundary-layer profiles, shape factor, and skin friction with direct numerical simulation (DNS) data and textbook equations for incompressible flat-plate flow are compared with predictions at low and high Reynolds numbers. A companion paper[8] discusses modeling of high Reynolds number transonic flow around a model simulating a single-engine configuration.[9–12] The separated flow on the nozzle boat-tail because of a shock-boundary-layer interaction is analyzed over a range of Reynolds numbers. Surface pressure coefficient distributions and integrated drag predictions on the afterbody are compared with experimental data with a Reynolds number range of 10–130 × 10^6. The computational sensitivity of viscous modeling and turbulence modeling are discussed.

Computational Procedure

Governing Equations

The general three-dimensional Navier–Stokes method PAB3D version 13S was used. This code has several computational schemes and different turbulence and viscous stress models.[4–7] The governing equations are the RANS equations obtained by neglecting all streamwise derivatives of the viscous terms. The resulting equations are written in generalized coordinates and conservative form. Viscous model options include thin-layer assumptions in j and k directions or calculations fully coupling both indices. Typically, the full three-dimensional viscous stresses are reduced to a thin-layer assumption, but this assumption must be made with caution. Experiments such as the investigation of supersonic flow in a square duct were found to require fully coupled two-directional viscosity to properly resolve the physics of the secondary crossflow.

The Roe upwind scheme with first-, second-, or third-order accuracy can be used in evaluating the explicit part of the governing equations, and the van Leer scheme is used to construct the implicit operator. The diffusion terms are centrally differenced, and the inviscid flux terms are upwind differenced. Two finite volume flux-splitting schemes are used to construct the convective flux terms. The code can utilize min–mod, van Albeda, Spekreijse–Venkat (S–V), or modified S–V (Ref. 13) limiters. All solutions were developed with the third-order-accurate scheme for the convective terms and second-order scheme for the viscous diffusion terms. Only the min–mod limiter was utilized for this study.

The code can utilize either a 2- or 3-factor numerical scheme to solve the flow equations. The 2-factor scheme is typically used as it requires 10–15% less memory than the 3-factor scheme. The memory difference is dependent on the size of cross-planes of the specific grid being used. When the 2-factor scheme is used, the orientation of the grid and predominant flow direction is typically along the i grid index, so that the Roe scheme is utilized to sweep streamwise through the computational domain, and the van Leer scheme is utilized for the solution of the cross-plane (i.e., i = const) of a three-dimensional problem. However, solving a single-cell-wide, two-dimensional mesh defined with the i direction of the grid oriented in the conventional streamwise direction will typically converge slower with the Roe relaxation solution scheme when compared with solving the equivalent problem with the van Leer scheme. Therefore, the i and j directions of a two-dimensional mesh are swapped, which allows the entire flowfield to be solved implicitly with each iteration. The explicit sweep is not used because only one cell exists in the i direction. The implicit scheme usually has a much higher rate of convergence and typically provides a solution that uses less computational time.

Turbulence Simulation

The turbulence model equations are uncoupled from the RANS equations and are solved with a different time step, typically one-half, from that of the principal flow solution. A considerably lower Courant–Friedrichs–Lewy (CFL) number is typically required to solve problems when both the main flow equations and turbulence equations are solved iteratively with identical time rates. Previously unpublished studies showed the larger time step differences (e.g., one-fourth to one-eighth slow solution convergence further, but result in identical final solutions. Flow solution transients occasionally require the turbulence equations time step to be reduced temporarily. Turbulence simulations are resolved at all grid levels, not just at the finest grid level.

Version 13S of the PAB3D code used in this study has options for several algebraic Reynolds stress (ASM) turbulence simulations. The standard model coefficients of the K-ε equations were used as the basis for all of the linear and nonlinear turbulent simulations.[14] Additionally, models using the eddy viscosity hypothesis produce inaccurate normal Reynolds stress differences.[4] Flat-plate flows, as well as other more complex aerodynamic flows, are anisotropic.

Successful implementation of the algebraic Reynolds stress models required the solution methodology for $\bar{P}$ of the underlying linear turbulence calculations to be modified. The PAB3D code was rewritten to solve for the stresses at the cell-face centers, which departs from the calculation of the turbulent stresses from derivatives of the cell-centered mean velocities. Previous (unpublished) attempts to implement nonlinear turbulence models in the context of a cell-centered eddy viscosity model worked only for two-dimensional problems and were unable to resolve three-dimensional flows.

Linear K-ε Equations

The transport equations for K and the dissipation rate are written as

$$\frac{\partial K}{\partial t} + u_k \frac{\partial K}{\partial x_k} = \bar{P} - \varepsilon + \frac{\partial}{\partial x_k}\left[\left(\nu^L + C_\mu \frac{K^2}{\varepsilon}\right)\frac{\partial K}{\partial x_k}\right] \tag{1}$$

$$\begin{aligned}\frac{\partial \varepsilon}{\partial t} + \bar{u}_k \frac{\partial \varepsilon}{\partial x_k} = {}& \frac{\partial}{\partial x_k}\left[\nu^L + C_\mu \frac{K^2}{\varepsilon}\right)\left.\frac{\partial \varepsilon}{\partial x_k}\right] \\ & + C_{\varepsilon 1}\frac{\varepsilon \bar{P}}{K} - C_{\varepsilon 2}\frac{\varepsilon}{K}\left[\varepsilon - 2\nu\left(\frac{\partial \sqrt{K}}{\partial n}\right)^2\right]\end{aligned} \tag{2}$$

where $\bar{P} = \tau^T_{ik}(\partial u_i/\partial x_k)$, $C_{\varepsilon 1} = 1.44$, $C_{\varepsilon 2} = 1.92$, $C_\mu = 0.090$.

The convective terms are solved with third-order differencing. The diffusion terms are solved using second-order central differencing. The damping function of Launder and Sharma,[15] $f_\mu = \exp[-3.41/(1 + R_T/50)^2]$, determined the behavior of ε near the wall as a function of $R_T = K^2/\nu\varepsilon$. The boundary conditions for ε and K at the wall are $\varepsilon_{\text{wall}} = 2\nu[(\partial/\partial n)\sqrt{K}]^2$ and $K_{\text{wall}} = 0$. The stress components in linear turbulence models are developed with laminar and turbulent components, $\tau_{ij} = \tau^L_{ij} + \tau^T_{ij}$. A generalization of Boussinesq's hypothesis redefines laminar and turbulent components as follows:

$$\tau^L_{ij} = A^L\delta_{ij} - 2\mu^L S_{ij} \tag{3}$$

where

$$A^L = \frac{2}{3}\mu^L S_{kk} \quad \text{and} \quad S_{ij} = \frac{1}{2}\left(\frac{\partial u_i}{\partial x_j} + \frac{\partial u_j}{\partial x_i}\right) \tag{4}$$

The turbulent component of the stresses τ_{ij}^T is represented by the sum of linear (T_l) and nonlinear (T_n) components. The linear stress is $\tau_{ij}^{T_l} = A^T\delta_{ij} - 2\mu^T S_{ij}$, where $A^T = \frac{2}{3}(\rho K + \mu^T S_{kk})$. The nonlinear component of the turbulent stresses are addressed in the following section.

For Shih et al.,[18] the form is

$$C_\mu^* = 1/[6.5 + A_s^*(U^*K/\varepsilon)] \tag{9}$$

For Gatski and Speziale,[3] the form is

$$C_\mu^* = \text{const} \times (1 + \chi^2)/(3 + \chi^2 + 6\chi^2\psi^2 + 6\psi^2) \tag{10}$$

A_s^*, U^*, χ, and ψ are all different functions of the strain and vorticity tensors and are detailed in the Appendix.

The C^* of Girimaji[18] is

$$G_1 = \begin{cases} L_0^1 L_2/[(L_1^0)^2 + 2\eta_2(L_4)^2] & \text{for} \quad \eta_1 = 0 \\ L_0^1 L_2/[(L_1^0)^2 + \frac{2}{3}\eta_1(L_3)^2 + 2\eta_2(L_4)^2] & \text{for} \quad L_1^1 = 0 \\ -\dfrac{p}{3} + \left(-\dfrac{b}{2} + \sqrt{D}\right)^{1/3} + \left(-\dfrac{b}{2} - \sqrt{D}\right)^{1/3} & \text{for} \quad D > 0 \\ -\dfrac{p}{3} + 2\sqrt{\dfrac{-a}{3}}\cos\left(\dfrac{\theta}{3}\right) & \text{for} \quad D < 0 \quad \text{and} \quad b < 0 \\ -\dfrac{p}{3} + 2\sqrt{\dfrac{-a}{3}}\cos\left(\dfrac{\theta}{3} + \dfrac{2\pi}{3}\right) & \text{for} \quad D < 0 \quad \text{and} \quad b > 0 \end{cases} \tag{11}$$

Nonlinear Turbulent Stress Equations

Three theories of explicit algebraic Reynolds stress models were used. Little data exist for implementing explicit ASM in a generalized three-dimensional Navier–Stokes method such as PAB3D. The model developed by Shih, Zhu, and Lumley[2] (SZL) is based on the turbulent constitutive relations developed by Shih and Lumely.[16] In theory, the Reynolds stresses are related to the mean velocity gradients, as well as K and ε. Gatski and Speziale[3] (GS) developed a set of algebraic relations between the turbulent Reynolds stresses and the mean velocity field that uses the pressure/strain relationship of Speziale et al.[17] The Girimaji model[18] (G) is based on the same theory as the GS model, except for the calculation of C_μ. The Reynolds stress contribution $\tau_{ij}^{T_n}$, used by Shih et al.,[2] is

$$\tau_{ij}^{T_n} = 2\beta(K^3/\varepsilon^2)(W_{ik}\bar{S}_{kj} - \bar{S}_{ik}W_{kj}) \tag{5}$$

by Gatski and Spezial[3] it is

$$\tau_{ij}^{T_n} = C_\mu^*(K^3/\varepsilon^2)[\beta_1(W_{ik}S_{kj} - S_{ik}W_{kj}) + \beta_2(S_{ik}S_{kj} - \tfrac{1}{3}S_{mn}S_{mn}\delta_{ij})] \tag{6}$$

by and Girimaji[18] it is

$$\tau_{ij}^{T_n} = 2C_\mu^*(K^3/\varepsilon^2)[-G_2(W_{ik}S_{kj} - S_{ik}W_{kj}) + G_3(S_{ik}S_{kj} - \tfrac{1}{3}S_{mn}S_{mn}\delta_{ij})] \tag{7}$$

where

$$W_{ij} = \frac{1}{2}\left(\frac{\partial u_i}{\partial x_j} - \frac{\partial u_j}{\partial x_i}\right)$$

$$\bar{S}_{ij} = S_{ij} - \tfrac{1}{3}S_{kk}\delta_{ij}$$

μ^T is defined as

$$\mu^T = C_\mu^*(\rho K^2/\varepsilon) \tag{8}$$

where $C_\mu^* = f_\mu C_\mu$ for solutions of linear turbulence simulations, or $C_\mu^* = f(S, W, K, \varepsilon)$ for solutions of algebraic Reynolds stress simulations. Functions for C_μ^* take the following forms for each of the ASM.

The variable G_1, utilized by Girimaji,[18] is equal to $-C_\mu^*$. A compilation of the parameters used in the Girimaji's model[18] can be found in the Appendix.

The solution processes for wall-bounded flows were equally robust for each of the models; i.e., CFL number ranges from 1 to 2. Previous results, not shown in this paper, show that the GS model required lower CFL numbers for the solution of free-shear flows; e.g., CFL numbers around 0.2. Obtaining converged solutions using Gatski's C_μ^* (Ref. 18), were found to be problem dependent. Girimaji's G_1 function[18] appears to be extremely well behaved, which allows the use of fairly high CFL numbers.

Turbulent Trip Equations

Placing K and ε profiles at user-specified lines or planes in the flowfield is the technique used for initializing the viscous flow transition from laminar to turbulent. The line or plane of the specified trip area is surveyed for the maximum and minimum velocity and vorticity along that line, and a shape function from 0 to 1 is created, $F = (f - f_{\min})/(f_{\max} - f_{\min})$, where f is a product of the velocity and vorticity $f = u|W|$, where $|W| = 2\sqrt{\Sigma\ W_{ij}^2}$. The turbulent kinetic energy profile is then $K = \alpha\bar{U}F$, where α is a free parameter that determines the magnitude of the impulse as a percent of local total velocity $\bar{U}$. The typical value specified by the user, and used for this paper, is 2% ($\alpha = 0.02$). The ε profile was developed from the assumption that production over dissipation is 1, that is, $\bar{P}/\varepsilon = 1$. This results in the equation $\varepsilon^2 = 2C_\mu K^2\bar{S}_{ij}(\partial u_i/\partial x_j)$. The result of the tripping is typically observed as a localized spike in the K field when viewing the solution. This turbulent profile then develops as dictated by the flow solution.

Solution Process

Turbulent flow solutions that use ASM and the two-equation linear K-ε model require 23 words of memory per grid point. The code speed is dependent on the turbulence model, viscous model assumptions, and numerical schemes. Table 1 contains the timing of some of the options available in the code for a C-90 in microseconds/iteration/grid point.

Several parameters were used to gauge solution convergence. Local skin friction, shape factor, and solution residual were monitored for convergence of the flat-plate solutions. Total afterbody drag, nozzle pressure drag, and solution residual were used to determine the solution status at the coarse (144), medium (122), and fine (111) grid levels of the axisymmetric

Table 1 Survey of code timing

Solver scheme	Viscous modeling[b]	Turbulence model	Stress center	Timing
2-factor	*j-k* thin	Girimaji ASM	Face	23
2-factor	*k* thin	Girimaji ASM	Face	20
Diag.[a]	*j-k* thin	Girimaji ASM	Face	16
Diag.[a]	*k* thin	Girimaji ASM	Face	14
2-factor	*k* thin	GS ASM	Face	19
2-factor	*k* thin	SZL ASM	Face	20
2-factor	*k* thin	Linear K-ε	Face	18
2-factor	*k* thin	Linear K-ε	Cell	17
Diag.[a]	*k* thin	Linear K-ε	Face	12

[a]Diagonalization. [b]Thin-layer uncoupled.

afterbody. The designation means divide the number of *i* cells by the first number, the number of *j* cells by the second number, and the number of *k* cells by the third number. Afterbody drag variance of less than 0.50% percent for approximately 500 iterations was achieved for all test cases.

The conservative patch interface package of Abdol-Hamid et al.[6] enables the code to properly transmit information between mismatched block interfaces. Integer-to-one interfaces are considered a subset of the arbitrary block interface and do not need to be specified as such to the patching code. However, note that features in the flow developed on one side of an interface should not be obliterated on the other side because of an excessive grid density mismatch.

Third-order continuity in transmitting the fluxes across block boundaries is maintained by the code; lower-order continuity may be specified by the user if required. As with most Navier–Stokes methods of this type, equal cell-size spacing on either side of an interface in directions normal to the interface should be maintained, regardless of the mesh sequencing level of the block.

Boundary Conditions

For this study, solid walls were treated as no-slip adiabatic surfaces. The solid wall boundary condition was satisfied by setting the momentum flux of the solid wall cell face to zero. A boundary condition for the Riemann invariants along the characteristics was specified for the freestream inflow face and the lateral freestream outer boundary of the flow domain. An extrapolation boundary condition was applied on the downstream outflow face. The axisymmetric flow assumption for the single-cell grids was implemented by placing flow symmetry conditions to the lateral side boundaries of the computational domain.

Results and Discussion

Flat-Plate Grid

The 5-m flat-plate multiblock grid had an H-type mesh topology, with the blocking in Fig. 1. The computational domain included an inflow block extending 1-m upstream from the leading edge of the 5-m flat plate. The initial streamwise grid spacing at the leading edge of the plate was 1.0×10^{-4} m and was exponentially stretched from the leading edge to the trailing edge at a rate of 5%, with a total of 161 grid points. The first cell height of the baseline grid was 1.0×10^{-6} m fixed at both ends of the plate and exponentially stretched from the surface to the outer boundary at a rate of 11%, with a total of 121 grid points. The upper boundary was 2 m away and the lateral width of the grid was 0.01 m. The baseline grid had all three blocks dimensioned at 81 × 121. Tripping to turbulent flow simulation occurred around $R_x = 0.3 \times 10^6$ or $R_{\delta_1} = 900$, which corresponds to a physical distance of approximately 9-mm downstream of the plate leading edge. This allowed for laminar flow to occur over roughly 32 computational cells (for the baseline grid) before tripping to turbulent flow. Grid cell counts were divisible by four to allow a minimum of two levels of grid sequencing. The effective expansion rate for the one-quarter grid would then be around 50% and be at a y^+ of approximately 3.5.

Boundary-Layer Characteristics

Figure 2 shows the Reynolds number based on length variation with distance from the leading edge. The Reynolds number at the plate trailing edge was approximately 180×10^6. Note that the plot is log–log with the symbols indicating the streamwise distribution of the grid points. The high Reynolds number was obtained by increasing the freestream total pressure, rather than physically lengthening the flat-plate geometry. The sensitivity of the boundary-layer profiles to grid density at $R_\theta \approx 1400$ and 1×10^5 are shown in Figs. 3 and 4. Additional grid sensitivities are shown for different quantities in Figs. 5–9. The von Kármán constant is determined from the inverse of the slope of the linear least-squares fit of all the boundary-layer profile points between $y^+ = 40$ and $y = 0.2\delta_1$. N_l is the number of points available for the least square fit at each streamwise station.

Two grid density studies were performed on the flat-plate configuration. The first was a boundary-layer cell density study that used five meshes. Grids were generated with vertical cell counts of 120, 60, 40, 30, and 20, starting with the same cell height and streamwise cell spacing. The second was a variation of the number of streamwise cells at 160, 80, 40, and 20, with the vertical cell count and spacing fixed.

The boundary-layer profiles for the five vertical density meshes for $R_\theta \approx 1400$ were fairly coincident until $k \approx 40$–30 meshes. The number of cells below $y^+ = 700$ are noted in Table 2.

A departure from the baseline grid profile occurs around 40 to 30 cells, which corresponds to 15 to 12 cells in the boundary layer. A similar, but not as strong conclusion occurs at the $R_\theta = \times 10^5$ plot (Fig. 4). An insufficient number of cells in the boundary layer begin to create errors in the solutions, as well as in the analysis of the solutions. As the number of points in the profile decrease and the size of the outer boundary-layer edge cells increase, the calculation of some profile properties

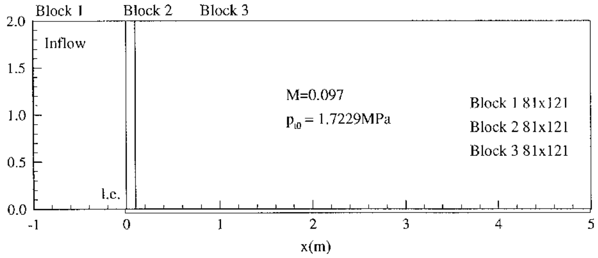

Fig. 1 Blocking and grid arrangement for subsonic flat plate.

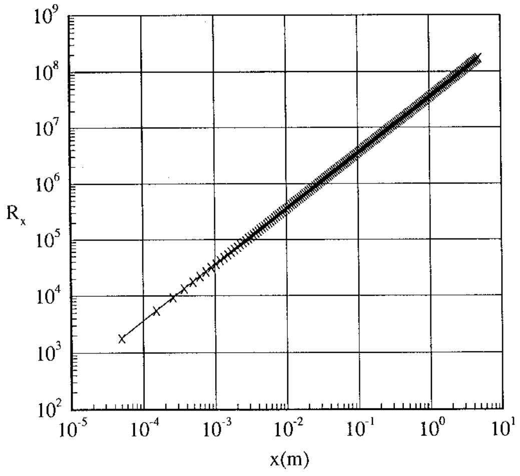

Fig. 2 Reynolds number with distance from leading edge.

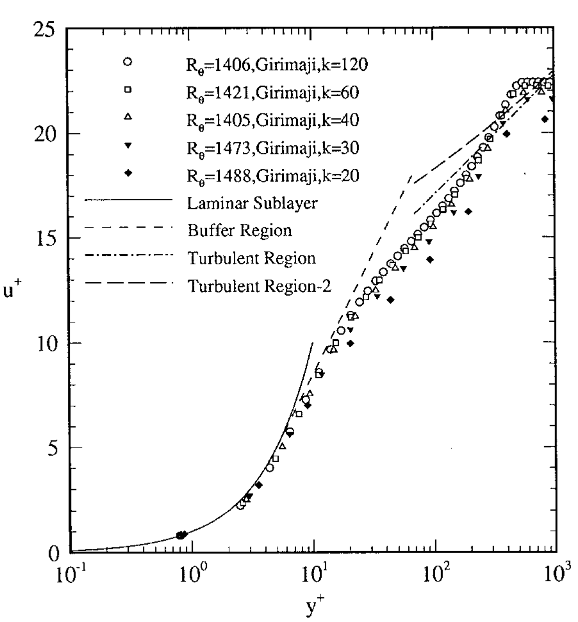

Fig. 3 Effect of vertical grid density on law-of-the-wall profiles at low R_θ

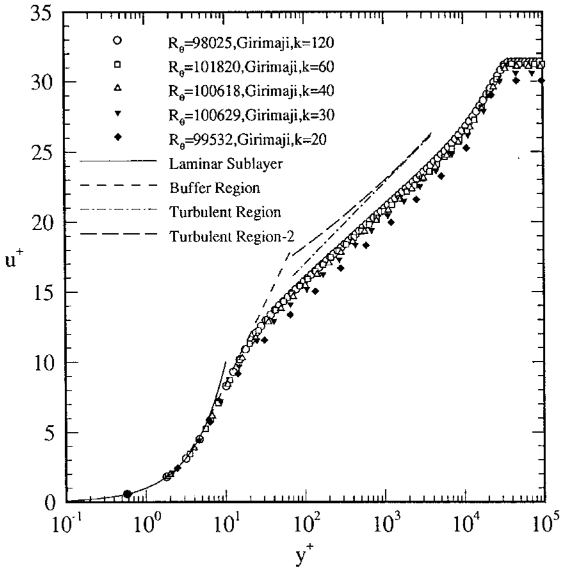

Fig. 4 Effect of vertical grid density on law-of-the-wall profiles at high R_θ

degrade. An example of this is shown in the predicted variation of the von Kármán constant with R_θ (Fig. 5). For values of R_θ greater than 10^3, there was little difference between the baseline mesh density and the $k = 60$ mesh. Even the $k = 30$ and 20 meshes were fairly close to the baseline mesh κ around $R_\theta = 2 \times 10^5$, though the numerical errors were considerable over the whole range of R_θ for those two grids as observed by the irregularity of the trend in κ. Not only were typically less than 10 points available to the linear fit, but the cells at the outer edge were large in relation to the boundary-layer thickness at that point, which created a stair-stepping effect in the analysis. Similarly, the skin friction correlation and H_{12} shape factor variation with R_θ (Fig. 6) show a waviness for the $k = 30$ and 20 meshes. The two finest meshes, $k = 120$ and 60, were fairly coincident for the whole range of R_θ. A cross-plot of the variation of local skin friction coefficient with a vertical grid count at three R_θ is shown in Fig. 7. Between 60–120 cells were required to attain grid convergence at all three stations.

Considerably less sensitivity was observed in the skin friction correlation and H_{12} shape factor for grids with fewer streamwise points (Fig. 8). Laminar flow was not established on the plate upstream of the transition point for the $j = 20$ streamwise cell mesh, and only three cells of laminar flow occurred for the $j = 40$ cell mesh. The 80 and 160 streamwise cell meshes were nearly coincident along both the laminar portion $R_\theta < 350$ and downstream of $R_\theta = 1000$. The two finer meshes had slight, but not significantly different transitional flows between the two values of R_θ. Additionally, the effect of streamwise grid on the variation of κ with R_θ is not significantly affected until the coarsest mesh $j = 20$ (Fig. 9).

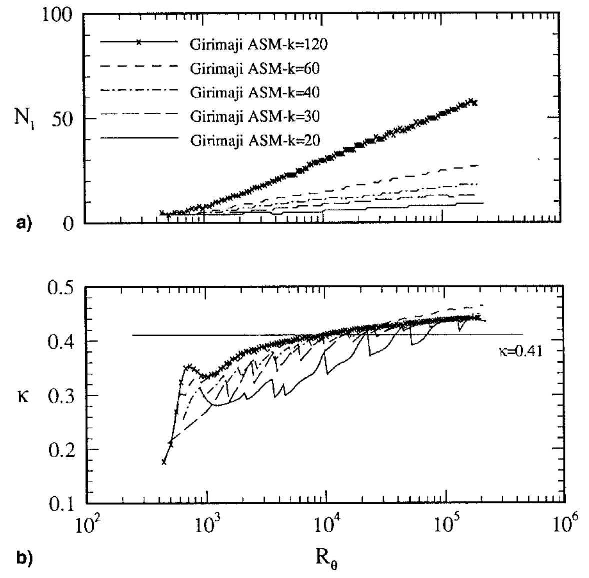

Fig. 5 a) Number of points in log-layer for von Kármán constant and b) effect of vertical cell density on von Kármán constant.

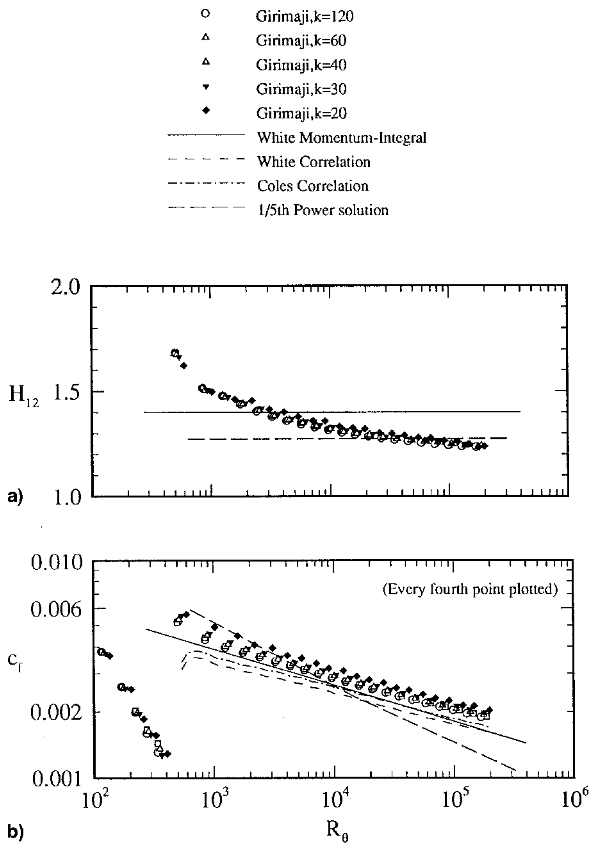

Fig. 6 a) Variation of shape factor and b) skin friction correlation with vertical cell density.

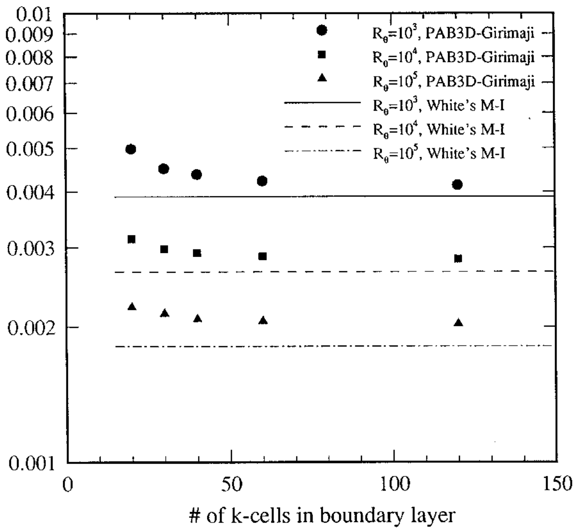

Fig. 7 Effect of cell density in boundary layer on local skin friction at three streamwise stations.

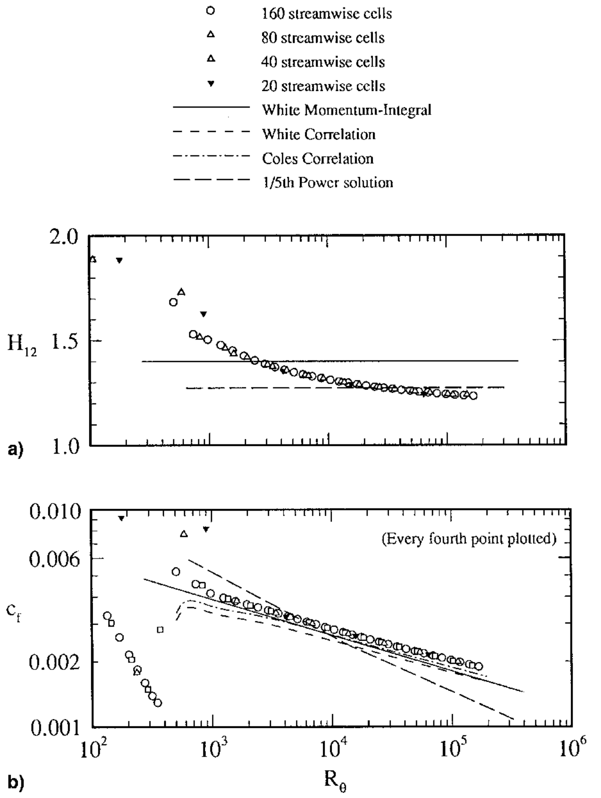

Fig. 8 a) Variation of shape factor and b) skin friction correlation with streamwise cell density using Girimaji ASM.

Table 2 Boundary-layer gridding

Vertical cell number	y_1^+	Number of cells in boundary layer
120	0.80	36
60	0.80	21
40	0.82	15
30	0.83	12
20	0.87	9

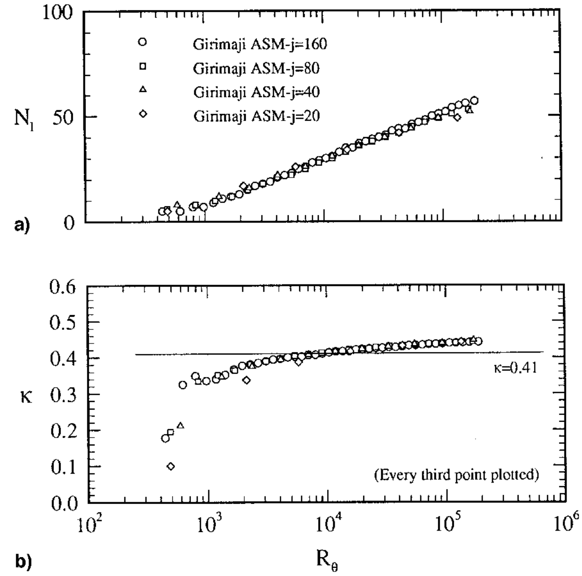

Fig. 9 a) Number of points in log-layer and b) effect of streamwise cell density on von Kármán constants.

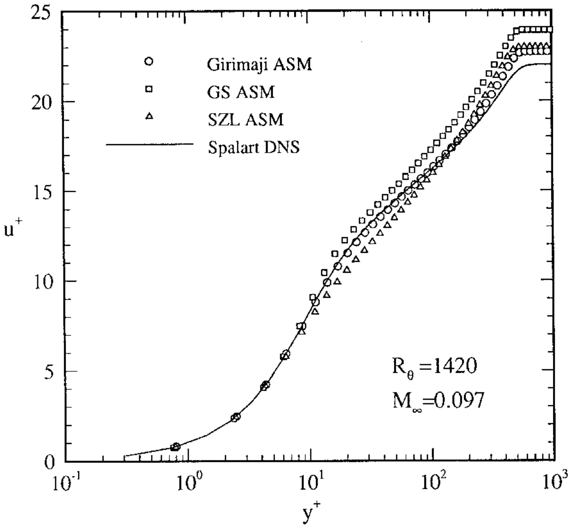

Fig. 10 Comparison of boundary-layer profiles for different turbulence models.

The normalized velocity and shear stress distributions at $R_\theta = 1420$ and 1×10^5 are shown in Figs. 10 and 11. The comparisons at $R_\theta = 1420$ are compared with the DNS calculations of Spalart[19] and at $R_\theta = 10^5$ are compared with the classical flat-plate equations. All three ASM fairly closely match the DNS calculation shown in Fig. 10, with the Girimaji model[18] following the closest in the buffer region and to the von Kármán constant of the DNS. All three models were slightly above the DNS at the edge of the boundary layer. Similarly, Girimaji[18] best fit the DNS turbulent stress profile, $u'v'^+ = (\partial u/\partial z)C_\mu f_\mu K^2/\varepsilon/u_\tau$, though all three ASM were generally a good match. The high Reynolds number comparisons shown in Fig. 12, at $R_\theta = 1 \times 10^5$, approximately $R = 90 \times 10^6$, have trends fairly consistent with the classical flat-plate boundary-layer flow equations. The stress profiles shown in Fig. 13 have similar lower level behavior below $y^+ = 50$ at the lower Reynolds number profiles and a greatly flattened region of constant stress below the boundary-layer edge around $y^+ = 3 \times 10^4$. The grid typically had two cells less than $y^+ = 2.5$ and about 36 cells in the boundary layer at $R_\theta = 1420$. The von Kármán constant from two empirical theories bracket the constant predicted from the model. Both SZL and GS were slightly below these levels. The turbulent shear stress shown in Fig. 13 has the slightly flattened profile that is consistent with extended

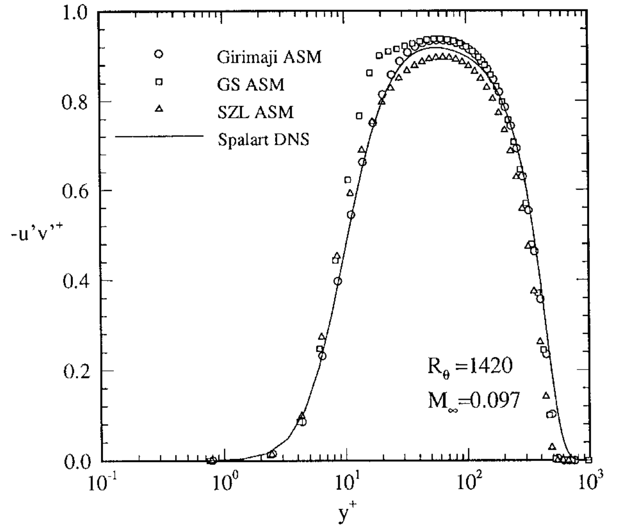

Fig. 11 Comparison of turbulent shear stress profiles for different turbulence models.

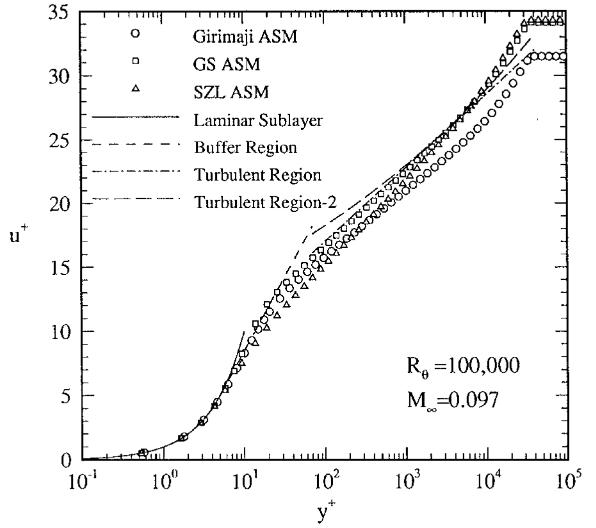

Fig. 12 Comparison of boundary-layer profiles for different turbulence models.

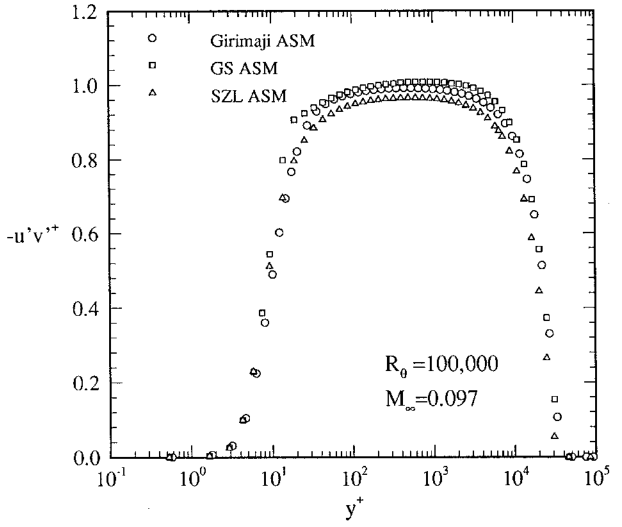

Fig. 13 Comparison of turbulent shear stress profiles for different turbulence models.

log-layer behavior of the high Reynolds number profile of Fig. 12.

Boundary-Layer Shape Factors

All three ASM have very similar shape factors H_{12} and H_{32} trends as shown in Figs. 14 and 15, respectively. The first eight or so computational cells were neither laminar nor turbulent flow as the solution developed. The subsequent 28 cells matched the theoretical laminar flow characteristics very closely. The theoretical turbulent shape factor was not closely achieved until around $R_x = 20 \times 10^6$. Even though transition from laminar flow occurred relatively quickly, formation of a turbulent shape factor close to the theoretical shape required some distance. All three models very closely match the turbulent shape factor of $H_{12} = 1.27$ at very high Reynolds numbers. Unexpectedly, SZH developed an H_{32} shape factor lower than both GS and G (Fig. 15). Similar trends tended to occur in solutions using GS and SZL ASM, whereas solutions using G ASM typically departed from these two.

Flat-Plate Skin Friction

Figures 16–18 are comparisons of classical flat-plate theories for local and average skin friction with the three ASM solutions and a comparison of predicted skin friction correlation with several empirical theories. The equations for the local skin friction comparisons were

$$c_f = \begin{cases} 0.664/\sqrt{R_x}, & \text{Blasius} \\ 0.0590 R_x^{-1/5} & \text{1/5-power law} \\ 0.455/\ell n^2(0.06R_x) & \text{White} \end{cases} \tag{12}$$

The equations for the average skin friction were

$$C_F = \begin{cases} 1.328/\sqrt{R_L} & \text{Blasius} \\ 0.455/[\log_{10}^{2.58}(R_L) - A/R_L] & \text{Transition} \\ 0.074R_L^{-1/5} - A/R_L & \text{1/5-power law} \\ 0.523/\ell n^2(0.06R_L) & \text{White} \end{cases} \tag{13}$$

where $A = R_{\text{crit}}(C_{F_t} - C_{F_l})$, $C_{F_l} = 1.328/\sqrt{R_{\text{crit}}}$, $C_{F_t} = 0.074(R_{\text{crit}})^{-1/5}$.

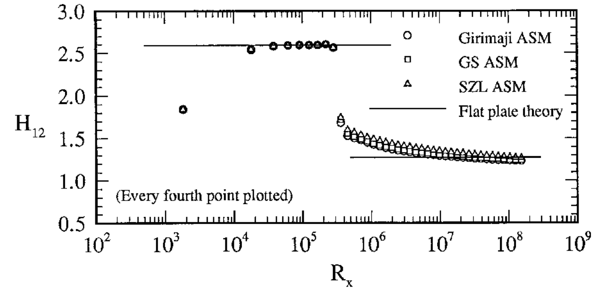

Fig. 14 Effect of turbulence model on H_{12} with local Reynolds number.

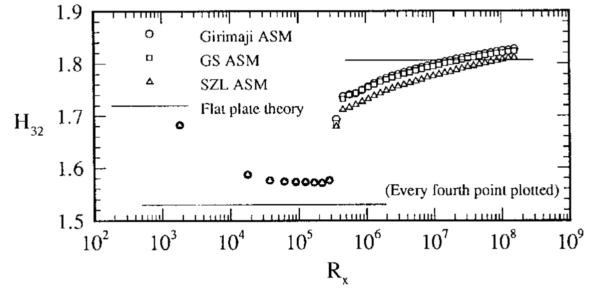

Fig. 15 Effect of turbulence model on H_{32} with local Reynolds number.

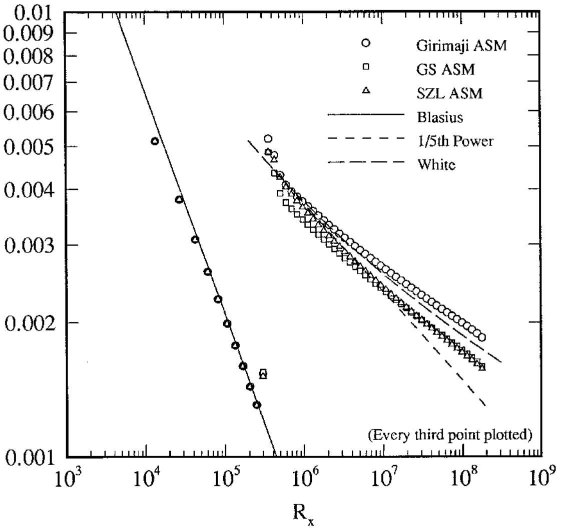

Fig. 16 Effect of turbulence model on local skin friction with Reynolds number.

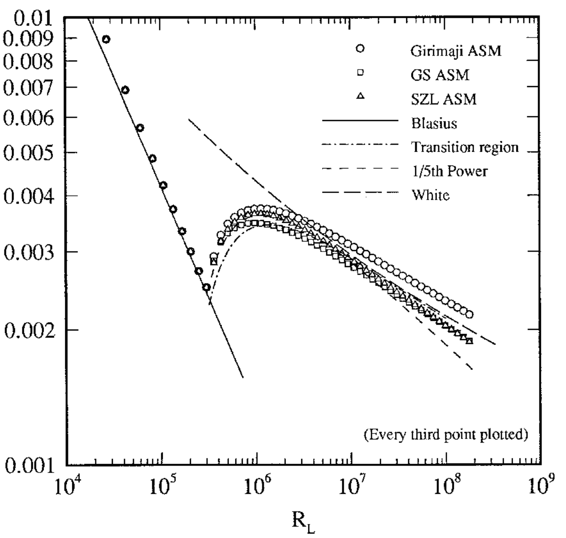

Fig. 17 Effect of turbulence model on average skin friction with Reynolds number.

R_{crit} is the local Reynolds number at the point of transition from laminar to turbulent flow. Transition was defined as the point at which the shape factor H_{12} first fell below 2.3.

The equations for the skin friction correlation follow.

White:

$$c_f = \frac{0.288e^{-1.37H_{12}}}{(\ell n\ R_\theta)^{1.753+0.283H_{12}}} \tag{14a}$$

von Kármán–Schoenherr:

$$1/c_f = 17.08\ \log_{10}^2 R_\theta + 25.11\ \log_{10} R_\theta + 6.012 \tag{14b}$$

Spaulding:

$$R_\theta = \frac{s^2}{6} + \frac{1}{\kappa E}\left[\left(1 - \frac{2}{\kappa s}\right)e^{\kappa s} + \frac{2}{\kappa s} + 1 - \frac{(\kappa s)^2}{6} - \frac{(\kappa s)^3}{12} - \frac{(\kappa s)^4}{40} - \frac{(\kappa s)^5}{130}\right] \tag{14c}$$

where $s = \sqrt{2/c_f}$, $\kappa = 0.4$ and $E = 12$.

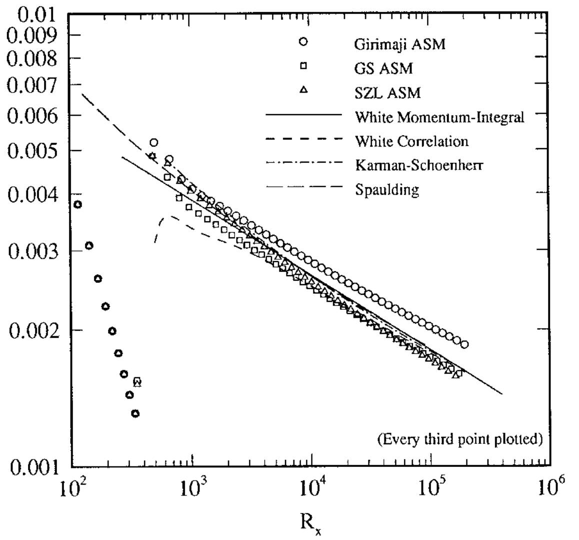

Fig. 18 Effect of turbulence model on skin friction correlation.

G, SZL, and GS ASMs predict similar and consistent skin friction characteristics throughout the Reynolds number range (Fig. 16). All three models were virtually identical in local and average skin friction for the laminar flow that developed upstream of the transition trip point at $R_x = 3 \times 10^5$. Downstream of the trip, the G model developed slightly higher local skin friction than the other two ASM, with subsequently higher average skin friction. All three models departed from the 1/5-power theory for local skin friction at Reynolds numbers above 20×10^6. The skin friction predicted by the G model was slightly above the higher Reynolds number theory of White, while the other two tracked slightly low.

The trend of average skin friction through transition to turbulent flow was similar between the three models and followed the 1/5-power theory very closely, until again departing around a Reynolds number of $20–30 \times 10^6$ (Fig. 17). Figure 18 is a plot of local skin friction with the Reynolds number based on momentum thickness. The G model skin friction correlation predicts the highest level of skin friction throughout most of the range of R_θ, although all three models are very similar in level and slope. Certain aspects of the local skin friction variation with R_θ are difficult to assess because of differences in the procedures used for the correlation. The CFD predicts a variation of both κ and H_{12} with R_θ. White's correlation assumes a constant κ for the range of applicability and developed a function for c_f using both R_θ and H_{12}. Von Kármán–Schoenherr and Spaulding have no explicit dependence of H_{12} in their equations and also appear to assume a constant κ throughout the range of R_θ.

Overall, all three nonlinear turbulence models appear to be consistent and have well behaved turbulent flat-plate properties up to Reynolds numbers of 180×10^6.

Summary

This class of advanced turbulence models in the PAB3D code were able to predict very high Reynolds number incompressible flat-plate flow. Prediction of the law-of-the-wall profile, von Kármán constant, and skin friction correlation require better than 15 cells ($k = 40$) in the boundary layer for a fixed $y^+ = 0.8$. Grid convergence of skin friction appeared to occur when 21 or more cells were in the boundary layer. Prediction of the law-of-the-wall profile, von Kármán constant, and skin friction correlation require more than 40 cells ($j = 40$) in the streamwise direction for a fixed $y^+ = 0.8$. Grid convergence of the skin friction correlation and the von Kármán constant appeared to occur when 80 or more streamwise cells were used. Differences in transition to turbulence are where the largest discrepancies occurred between the different streamwise grid densities. The low Reynolds number law-of-the-wall and turbulent stress profiles compared well with the Spalart DNS calculation. The high Reynolds number profiles retained similarity with elongation of the log–layer region. Local and average skin friction, shape factors, and skin friction correlations were consistent up to high Reynolds numbers when compared with classical and empirical theories.

Appendix: ASM Equation Parameters

The following functions and variables were used in the algebraic Reynolds stress models.

Used by the SZL model:

$$C_\mu^* = 1 \Bigg/ \left(6.5 + A_s^* \frac{U^*k}{\varepsilon}\right)$$

$$A_s^* = \sqrt{6}\cos(\phi)$$

$$\phi = \frac{1}{3}\cos^{-1}(\sqrt{6}W^*)$$

$$S^* = \sqrt{S_{ij}^* S_{ij}^*}$$

$$S_{ij}^* = S_{ij} - \frac{1}{3} S_{kk}\delta_{ij}$$

$$\Omega^* = \sqrt{\Omega_{ij}^* \Omega_{ij}^*}$$

$$\Omega_{ij}^* = \Omega_{ij} = \frac{1}{2}\left(\frac{\partial u_i}{\partial x_j} - \frac{\partial u_j}{\partial x_i}\right) = -\Omega_{ij}$$

$$W^* = S_{ij}^* S_{jk}^* S_{ki}^* / (S^*)^3$$

$$U^* = \sqrt{S_{ij}^* S_{ij}^* + \Omega_{ij}^* \Omega_{ij}^*}$$

$$\beta = \sqrt{1 - 9C_\mu^2 \left(\frac{S^*K}{\varepsilon}\right)^2} \Bigg/ \left(1 + 6\,\frac{S^*K}{\varepsilon}\,\frac{\Omega^*K}{\varepsilon}\right)$$

Used by the GS model:

$$\chi^2 = S_{ij}^* S_{ij}^* \qquad \psi^2 = \Omega_{ij}^* \Omega_{ij}^*$$

$$S_{ij}^* = \frac{g}{2}(2 - C_3)\frac{S_{ij}K}{\varepsilon}$$

$$\Omega_{ij}^* = \frac{g}{2}(2 - C_3)\frac{\Omega_{ij}K}{\varepsilon}$$

$$\bar{P}/\varepsilon = \frac{C_{\varepsilon_2} - 1}{C_{\varepsilon_1} - 1}$$

$$g = \left(\frac{C_1}{2} + \frac{\bar{P}}{\varepsilon} - 1\right)^{-1}$$

$$\alpha = g\left(\frac{4}{3} - C_2\right)$$

$$\beta_1 = g(2 - C_4) \qquad \beta_2 = 2g(2 - C_3)$$

$$C_1 = 3.4 + \frac{\bar{P}}{\varepsilon} \qquad C_2 = 0.368 \qquad C_3 = 1.25 \qquad C_4 = 0.4$$

$$C_{\varepsilon_1} = 1.44 \qquad C_{\varepsilon_2} = 1.83$$

Used by the G model:

$$L_1^0 = \frac{C_1^0}{2} - 1 \qquad L_1^1 = C_1^1 + 2$$

$$L_2 = \frac{C_2}{2} - \frac{2}{3} \qquad L_3 = \frac{C_2}{2} - 1 \qquad L_4 = \frac{C_4}{2} - 1$$

$$\eta_1 = \left(\frac{K}{\varepsilon}\right)^2 S_{mn}S_{mn} \qquad \eta_2 = \left(\frac{K}{\varepsilon}\right)^2 W_{mn}W_{mn}$$

$$p = -\frac{2L_1^0}{\eta_1 L_1^1} \qquad r = -\frac{L_1^0 L_2}{(\eta_1 L_1^1)^2}$$

$$q = \frac{1}{(\eta_1 L_1^1)^2}\left[(L_1^0)^2 + \eta_1 L_1^1 L_2 - \frac{2}{3}\eta_1 (L_3)^2 + 2\eta_2 (L_4)^2\right]$$

$$a = \left(q - \frac{p^2}{3}\right) \qquad b = \frac{1}{27}(2p^3 - 9pq + 27r)$$

$$D = \frac{b^2}{4} + \frac{a^3}{27} \cos(\theta) = \frac{-b/2}{\sqrt{-a^3/27}}$$

The coefficients G_2 and G_3 are

$$G_2 = \frac{-L_4 G_1}{L_0^1 - \eta_1 L_1^1 G_1} \qquad G_3 = \frac{2L_3 G_1}{L_0^1 - \eta_1 L_1^1 G_1}$$

additionally

$$C_1^0 = 3.4 \quad C_1^1 = 1.8 \quad C_2 = 0.36 \quad C_3 = 1.25 \quad C_4 = 0.4$$

References

[1] Launder, B. E., Reece, G. J., and Rodi, W., "Progress in the development of a Reynolds Stress Turbulence Closure," *Journal of Fluid Mechanics*, Vol. 68, 1975, pp. 537–566.

[2] Shih, T.-H., Zhu, J., and Lumley, J. L., "A New Reynolds Stress Algebraic Model," NASA TM-166644, Inst. for Computational Mechanics, 94-8, 1994.

[3] Gatski, T. B., and Speziale, C. G.,"On Explicit Algebraic Stress Models for Complex Turbulent Flows," NASA CR-189725, Inst. for Computer Applications in Science and Engineering, 92-58, Nov. 1992.

[4] Abdol-Hamid, K. S., Carlson, J. R., and Lakshmanan, B., "Application of Navier-Stokes Code PAB3D to Attached and Separated Flows for Use with *K*-ε Turbulence Model," NASA TP-3480, Jan. 1994.

[5] Abdol-Hamid, K. S., "A Multiblock/Multizone Code (PAB3D-v2) for the Three-Dimensional Navier-Stokes Equations: Preliminary Applications," NASA CR-182032, Oct. 1990.

[6] Abdol-Hamid, K. S., Carlson, J. R., and Pao, S. P., "Calculation of Turbulent Flows Using Mesh Sequencing and Conservative Patch Algorithm," AIAA Paper 95-2336, July 1995.

[7] Abdol-Hamid, K. S., "Implementation of Algebraic Stress Model in a General 3-D Navier-Stokes Method (PAB3D)," NASA CR-4702, Dec. 1995.

[8] Carlson, J. R., "Applications of Agebraic Reynolds Stress Turbulence Models Part 2: Transonic Shock-Separated Afterbody," *Journal of Propulsion and Power*, Vol. 13, No. 5, 1997, pp. 620–628.

[9] Reubush, D. E., and Putnam, L. E., "An Experimental and Analytical Investigation of the Effect on Isolated Boattail Drag of Varying Reynolds Number up to 130 × 10^6," NASA TND-8210, May 1976.

[10] Reubush, D. E., "The Effect of Reynolds Number on Boattail Drag," AIAA Paper 75-63, Jan. 1975.

[11] Reubush, D. E.,"The Effect of Reynolds Number on Boattail Drag of Two Wing-Body Configurations," AIAA Paper 75-1294, Sept. 1975.

[12] Reubush, D. E., "Experimental Investigation to Validate Use of Cryogenic Temperatures to Achieve High Reynolds Numbers in Boattail Pressure Testing," NASA TM X-3396, Aug. 1976.

[13] Krist, S. L., Thomas, J. L., Sellers, W. L, and Kjelgaard, S. O., "An Embedded Grid Formulation Applied to a Delta Wing," AIAA Paper 90-0429, Jan. 1990.

[14] Patel, V. C., Rodi, W., and Scheuerer G., "Turbulence Models for Near-Wall and Low Reynolds Number Flows: A Review," *AIAA Journal*, Vol. 23, No. 9, 1985, pp. 1308–1319.

[15]Launder, B. E., and Sharma, B. I., ‘‘Application of the Energy Dissipation Model of Turbulence to the Calculation of Flow near a Spinning Disk,’’ *Letters in Heat and Mass Transfer*, Vol. 1, 1974, pp. 131–138.

[16]Shih, T.-H., and Lumley, J. L., “Remarks on Turbulent Constitutive Relations,” NASA TM-106116, May 1993.

[17]Speziale, C. G., Sarkar, S., and Gatski, T. B., ‘‘Modeling the Pressure-Strain Correlation of Turbulence: An Invariant Dynamical Systems Approach,’’ *Journal of Fluid Mechanics*, Vol. 227, 1991, pp. 245–272.

[18]Girimaji, S. S., “Fully-Explicit and Self-Consistent Algebraic Reynolds Stress Model,’’ Inst. for Computer Applications in Science and Engineering, 95-82, Dec. 1995.

[19]Spalart, P. R., “Direct Simulations of Turbulent Boundary Layers up to $Re_\theta = 1420$,” *Journal of Fluid Mechanics*, Vol. 187, 1988, pp. 61–98.